Nanoscale

REVIEW

View Article Online
View Journal | View Issue

Check for updates

Cite this: *Nanoscale*, 2022, **14**, 17119

Tip-enhanced nanoscopy of two-dimensional transition metal dichalcogenides: progress and perspectives

Jiaqi Shao[a] and Weitao Su *[b]

Received 5th September 2022,
Accepted 7th November 2022

DOI: 10.1039/d2nr04864g

rsc.li/nanoscale

The optoelectronic properties of two-dimensional (2D) transition metal dichalcogenide (TMD) thin layers prepared by exfoliation or chemical vapour deposition are strongly modulated by defects at the nanoscale. The mediated electronic and optical properties are expected to be spatially localised in a nanoscale width neighbouring the defects. Characterising such localised properties requires an analytical tool with nanoscale spatial resolution and high optical sensitivity. In recent years, tip-enhanced nanoscopy, represented by tip-enhanced Raman spectroscopy (TERS) and tip-enhanced photoluminescence (TEPL), has emerged as a powerful tool to characterise the localised phonon and exciton behaviours of 2D TMDs and heterojunctions (HJs) at the nanoscale. Herein, we first summarise the recent progress of TERS and TEPL in the characterisation of several typical defects in TMDs, such as edges, wrinkles, grain boundaries and other defects generated in transfer and growth processes. Then the local strain and its dynamic control of phonon and exciton behaviours characterised by TERS and TEPL will be reviewed. The recent progress in characterising TMD HJs using TERS and TEPL will be subsequently summarised. Finally, the progress of TERS and TEPL combined with optoelectronic sensitive electronic scanning probe microscopy (SPM) in the applications of TMDs will be reviewed.

Published on 17 November 2022. Downloaded by Yunnan University on 8/14/2025 5:32:42 PM.

Introduction

In recent years, TMDs composed of periodic layers of transition metals and chalcogenide elements have emerged as a new class of optoelectronic materials owing to their unique physical properties such as high electron mobility,[1] large exciton binding energy,[2] large spin–orbit splitting energy,[3] *etc*. Defects, such as vacancies,[4] grain boundaries,[5] dislocations,[6,7] nonstoichiometric fluctuations,[8] wrinkles,[9] organic residues,[10] *etc*., are crucial factors affecting the electronic and optical properties of monolayer (1L) TMDs and their HJs and twisted thick layers. For TMD HJs, interlayer diffusion and the resulting interfacial alloying effect can also be classified as a general defect. Considering the small exciton diffusion length (a few hundreds of nanometres)[11] in TMDs, the modulated electronic and optical behaviours are expected to be spatially localised in a nanoscale width neighbouring the defects.[13] Characterising the electron and exciton behaviours in such a small scale challenges the spatial resolution, sensitivity and functionalities of many analytical tools. It is known that the conventional electrical probe method only gives averaged electronic properties in a spatial width of dozens of microns.[5] Far field Raman or photoluminescence (PL) mapping is only able to provide averaged spectral information in a spatial width of hundreds of nanometres due to the optical diffraction limit.[12] Abbreviation-corrected transmission electron microscopy (TEM) is able to give the atomic structure of defects with a spatial resolution of picometer scale,[13] whereas the obtained atomic structure is very hard to be directly correlated with the local electrical, optoelectronic or optical properties.

Tip-enhanced nanoscopy has recently emerged as a promising tool to examine the microstructure modification and local excitonic behaviours of TMDs at the nanoscale. Raman and PL signals of a sample can be strongly enhanced by a sharp metallic tip *via* localised surface plasmon and lightning rod effects, resulting in TERS and TEPL, respectively.[14] The lattice vibration, doping effect, excitonic characteristics, *etc*. are expected to be obtained by analysing the tip-enhanced Raman and PL spectra at the nanoscale. TERS and TEPL have been successfully implemented in characterising the microstructure and defects of a variety of 2D materials,[15–29] such as WSe_2,[21,26] WS_2,[16,19,28,29] MoS_2,[17,25,27] and HJs.[30–33] However, to the best of our knowledge, there are few review literatures that summarise the recent studies of TERS and TEPL of TMDs. Therefore, a comprehensive review of the recent progress is still in demand.

[a]*College of Materials and Environmental Engineering, Hangzhou Dianzi University, Hangzhou, 310018, China*
[b]*School of Sciences, Hangzhou Dianzi University, Hangzhou, 310018, China. E-mail: suweitao@hdu.edu.cn*

Published on 17 November 2022. Downloaded by Yunnan University on 8/14/2025 5:32:42 PM.

This manuscript is organized as follows. First, a brief introduction of the theory and instrumentation of tip-enhanced nanoscopy will be presented. The challenges in the measurements of TMDs will also be discussed. Then we will summarise the recent progress of TERS and TEPL in the characterisation of edges, wrinkles, grain boundaries and other defects of TMDs generated in transfer and growth processes. The characterisation of local strain and its dynamic control characterised by TERS and TEPL will be further summarised. Next, we will review the applications of TERS and TEPL in the characterisation of TMD HJs. Finally, the TERS and TEPL and electrical SPM combined method and its applications in TMDs will also be reviewed. This review will be helpful to understand the exciton and phonon behaviours of TMDs at the nanoscale and further understand the localised optoelectronic properties of TMD materials.

Tip-enhanced nanoscopy: principles and instrumentation

Principles of tip-enhanced nanoscopy

Tip-enhanced nanoscopy is a characterising tool that utilizes the localised surface plasmon resonance (LSPR), tip–substrate coupling and lighting rod effects of a plasmonic tip to obtain higher spatial resolution and stronger signal intensity than far field (FF) Raman or PL spectroscopy. Usually, a sharp Ag or Au metallic or metal coated SPM tip is positioned at the focus centre of an excitation laser. Owing to the LSPR and lighting rod effects provided by this plasmonic tip, the electric field intensity beneath the tip apex will be strongly enhanced, resulting in selectively enhanced Raman or PL signals of a sample placed under the tip apex.[34]

LSPR effect

The LSPR effect refers to the enhancement of the electric field intensity caused by the collective oscillation of free electrons of the metallic tip apex under the excitation of incident light and the formation of a localised additional electric field (Fig. 1a). The scattering cross section of a nanosphere, defined as the ratio of the scattered electric field to the incident field, can be expressed as eqn (1):[34,35]

$$\sigma_s = \frac{k^4}{6\pi{\varepsilon_0}^2}|\alpha(\omega)|^2 \quad (1)$$

where k is the wave vector and ε_0 is the dielectric constant of vacuum. The electric permittivity $\alpha(\omega)$ can be expressed as:[35]

$$\alpha(\omega) = 4\pi\varepsilon_0 R^3 \frac{\varepsilon(\omega) - \varepsilon_0}{\varepsilon(\omega) + 2\varepsilon_0} \quad (2)$$

where R is the diameter of a nanosphere and $\varepsilon(\omega) = \varepsilon_r + i\varepsilon_i$ is the complex dielectric constant of a nanosphere.

The electric permittivity in eqn (2) is maximized when the denominator $\varepsilon(\omega) + 2\varepsilon_0 = 0$, *i.e.*, $\varepsilon_i(\omega) = 0$ and $\varepsilon_r(\omega) = -2\varepsilon_0$, resulting in an infinite scattering cross section according to eqn (1). When the frequency of incident light satisfies the dielectric resonant conditions of a probe according to eqn (1) and (2), the electric field intensity beneath the tip apex will be most effectively enhanced, which is the so-called LSPR effect.[35] The LSPR resonant wavelength of a plasmonic tip strongly depends on the dielectric constant, curvature and roughness of the tip, and it can be further modulated by controlling these parameters. In the visible light range, gold and silver are the most commonly used metals to prepare scattering metal probes. The resonant peak of an Au probe is in the red light range, while the Ag probe is located in the yellow to green light range[36] (Fig. 1b).

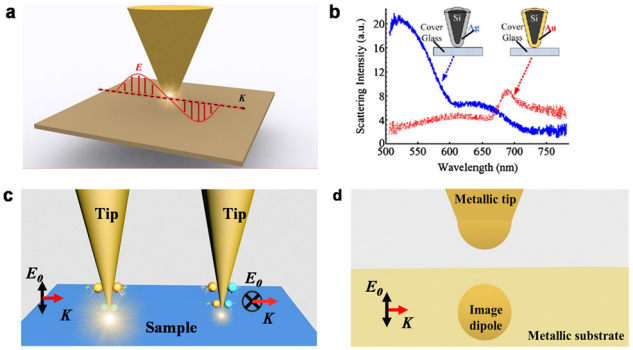

Fig. 1 (a) LSPR effect of an incident light wave (electric field amplitude ***E*** and wave vector ***K***) for a plasmonic probe; (b) scattering intensity of light as a function of the light wavelength measured for silver- and gold-coated silicon AFM probes;[36] (c) lighting rod effect of incident light polarization (***E***) parallel or perpendicular to the axis of plasmonic tips; and (d) imaging dipole effect of a plasmonic probe placed on the surface of a metallic substrate. (b) has been adapted/reproduced from ref. 36 with permission from IOP Publishing, copyright 2010.

Lightning rod effect

The lightning rod effect is generated by the accumulation of a high density of local surface charges at the singularity points of a metallic object. When the polarization direction of incident light is parallel to the axis of a plasmonic probe, the surface charge distribution is almost rotationally symmetrical under the influence of the applied electric field, and the charge density at the tip apex is strongly enhanced (Fig. 1c).[37,38] This results in a significantly enhanced local electric field beneath the tip. It should be noted that when the polarization direction of incident light is perpendicular to the axis of the plasmonic probe, charge accumulation is very weak at the tip apex, resulting in weak enhancement of the local electromagnetic field.

Imaging dipole effect

Compared with the case without a substrate, when a smooth gold or silver thin film is used as a substrate, the local electric field intensity under the tip apex is more tightly localised at the gap between the tip apex and the substrate, and a significant additional enhancement is expected to be obtained. This working mode is the so-called gap mode.[39] In the electric field

 This journal is © The Royal Society of Chemistry 2022

Published on 17 November 2022. Downloaded by Yunnan University on 8/14/2025 5:32:42 PM.

of the incident laser, the strong coupling of a local electric field of the tip apex to the metallic substrate can be modelled by a spherical imaging dipole placed at a mirror position of the tip apex (Fig. 1d). The additional permittivity provided by the imaging dipole can be expressed as

$$\alpha_{\text{image}} = \alpha \frac{\varepsilon_s - \varepsilon_0}{\varepsilon_s + \varepsilon_0} \quad (3)$$

where ε_s is the dielectric constant of the metallic substrate.

Enhancement factor

The effectiveness of a tip-enhanced nanoscopic measurement is usually quantified by contrast (C) and the enhancement factor (EF). Contrast refers to the intensity ratio of a target peak when the tip is in contact with and retracted from the sample surface, respectively, which is defined as[40]

$$C = \frac{I_{\text{tip-in}}}{I_{\text{tip-off}}} - 1 \quad (4)$$

where $I_{\text{tip-in}}$ and $I_{\text{tip-off}}$ are target peak intensities measured with the tip in contact with and retracted from the surface, respectively.

EF, on the other hand, includes the spatial volume of the incident excitation area as a parameter to quantify the enhancement effect of a nanoscopic system[41]

$$\text{EF} = \left(\frac{I_{\text{tip-in}}}{I_{\text{tip-off}}} - 1\right) \frac{V_{\text{FF}}}{V_{\text{NF}}} \quad (5)$$

where V_{FF} is the volume of the far field excitation region of incident light. V_{NF} is the effective volume of the localised electric field beneath the tip apex. Usually, the thickness of 1L 2D materials like MoS_2 or WS_2 is limited to several atom layers,[42] which is negligible compared with the diameter of laser focus (usually several hundreds of nanometres). Therefore, in the calculation of the EF of 2D materials, we can always ignore the thickness difference between V_{EF} and V_{FF} by using[41]

$$\text{EF} = \left(\frac{I_{\text{tip-in}}}{I_{\text{tip-off}}} - 1\right) \frac{A_{\text{FF}}}{A_{\text{NF}}} \quad (6)$$

where A_{FF} is the area of far field laser focus. A_{NF} is the effective area of the localised electric field, usually calculated from the tip diameter or the spatial resolution obtained from nanoscopy imaging using a given probe.[25,41]

In the enhanced local electric field, the correlation of Raman enhancement with the electric intensity is straightforward since the Raman enhancement factor is proportional to the fourth power of the ratio of the local electric intensity to the incident electric intensity ($|E_{\text{local}}/E_{\text{in}}|^4$),[43] whereas the analysis of PL enhancement is quite complicated. Both the generation and recombination rates of excitons can be strongly enhanced in the localised electric field.[25] However, the PL intensity is also affected by the Auger process related to the PL quenching effect. The metallic surface of a plasmonic tip acts as a shortcut for exciton recombination. The exciton might recombine *via* this nonradiative process by giving its energy to the third electron travelling in the tip apex, resulting in a lowered PL intensity compared to the conditions without the Auger process.[44]

Moreover, charge transfer between the tip and TMDs induces a $p(n)$ doping effect when the work function of the metallic tip is smaller (larger) than that of the TMD thin layer. The depletion (injection) of electrons in the TMD thin layer will induce the enhanced density of neutral excitons (trions). This will finally tune the relative PL intensity of neutral excitons and trions in the obtained TEPL spectrum.[25] Since the exciton generation and recombination of 1L TMDs take place in a thickness of the entire layer, the influences of the Auger process and charge transfer induced by the tip apex are much stronger than the conditions of a bulk semiconductor and cannot be neglected.

Instrumentation of tip-enhanced nanoscopy

According to the different configurations of illumination/collection optical paths referring to the plasmonic tip, the instruments of tip-enhanced nanoscopy can be usually classified into the following types: side illumination, top illumination and bottom illumination.

Side illumination

As for a side illumination configuration (Fig. 2a), the incident laser and the plasmonic probe are located at the same side of the sample. A linearly polarized laser beam is usually focused onto a side of the probe apex through a long working distance objective lens. The excited PL or Raman signals are enhanced by the plasmonic tip and collected by the same objective lens. In the side illumination configuration, it is easy to tune the polarization direction of the incident beam parallel to the tip axis, benefiting to form a longitudinal electric field with stronger enhancement.[45] Moreover, there is no limitation of the transparency of the substrate or the sample. However, the numerical aperture of a long working distance objective lens is

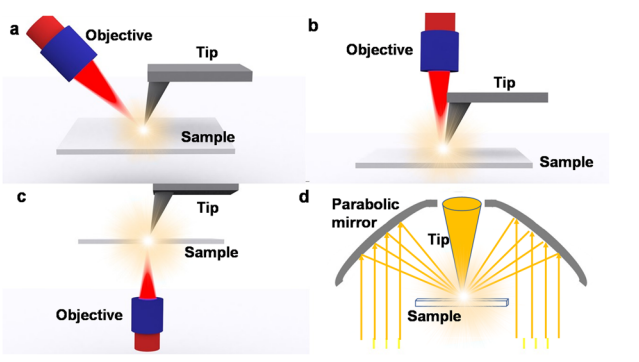

Fig. 2 Schematic of TERS configurations. (a) Side illumination; (b) top illumination; (c) bottom illumination; and (d) side illumination based on a parabolic mirror.

Published on 17 November 2022. Downloaded by Yunnan University on 8/14/2025 5:32:42 PM.

usually less than 0.7, which limits the collection efficiency of light. In addition, in the side illumination configuration, the focus spot is projected onto the sample surface at an inclined angle ~30°,[45] resulting in a large elliptical focus shape and larger far field background noise.

Top illumination

In a top illumination configuration (Fig. 2b), the incident laser beam is focused onto a side of the plasmonic probe apex through a long working distance objective lens directly positioned above the sample. The excited Raman or PL signals are enhanced by the probe apex and then collected by the same objective lens. Usually a long working distance objective lens and a nose type probe are used to reduce light shielding of the probe shaft. In this configuration, the SPM system usually needs to be specially designed to fit a large size objective lens. Moreover, the shielding effect of the probe shaft on both the incident and collection beams needs to be considered.[46,47]

Bottom illumination (transmission mode)

As show in Fig. 2c, a plasmonic probe is placed on the top side of a sample. The laser beam penetrates the substrate and sample and is focused onto the tip apex from the bottom side of the substrate *via* a high NA objective lens. The PL or Raman signals are collected by using the same objective lens. In this configuration, an objective lens with a high numerical aperture of >1.3 can be used to effectively collect the PL or Raman signals in a larger angle range. However, since both the illuminated and collected beams need to penetrate the substrate and sample, transparent or semitransparent samples and substrates are required in the measurements.[14,18,48]

Side illumination based on a parabolic reflector

In this configuration, the incident laser beam is focused onto the apex of a plasmonic probe *via* a parabolic mirror. The excited PL or Raman signals are collected by the same parabolic mirror and sent into the detector. The parabolic mirror effectively increases the spatial solid angle range of excitation and collection beams and improves the illumination and collection efficiency (Fig. 2d).[49,50] However, the parabolic mirror needs to be specially designed and processed to fit the SPM system.

Considering the optical configuration of the TERS system, the sample preparation procedures of TMDs need to be optimized. The transmission of 1L TMDs is >94.5%,[51] which allows the observation of TERS and TEPL using a bottom illumination system. In order to allow the transmission of incident and scattered photons, a transparent substrate is also required. However, directly depositing high quality 1L or few-layer TMDs on a commonly used glass or quartz coverslip is greatly restricted due to the large density of nucleation sites.[52] A mechanical exfoliation method would be alternatively desirable to obtain high quality thin layer flakes on a glass or quartz substrate. For a lateral or top illumination system, the substrate can be either transparent or opaque, which is desirable for the observation of the intrinsic defects of TMDs directly grown on SiO_2/Si substrates using the CVD method. In a gap mode TERS system, a gold or silver thin film is required to be placed between the few-layer TMD flakes and the substrate. However, direct deposition of high quality 1L TMD flakes on a gold or silver surface using CVD is greatly restricted.[19] As an alternative, a wet or dry transfer method can be used to prepare few-layer TMDs or their HJs. Transfer introduced defects, such as organic residues, bubbles, wrinkles, *etc*.[55] may strongly affect the physical properties of the samples and need to be diminished.

Characterisation of the deposition and transfer induced defects of 2D TMD thin layers by tip-enhanced nanoscopy

For most TMD semiconductors, excitation is the dominant transition process of light emission. In 1L TMDs such as MoS_2 with a perfect lattice structure, the distribution of excitons is expected to be uniform, which is expected to induce uniform PL intensities of different excitons over the entire flake. However, the prepared TMD thin layer samples always contain certain defects and consequently nonuniform exciton PL intensity distribution is expected to be observed. As early as 2016, Su *et al.* successfully used TERS and TEPL to investigate mechanically exfoliated MoS_2 thin layers.[25] They studied the charge transfer effects between metallic (Ag and Au) coated TERS tips and 1L MoS_2. The related influences to the local exciton process and electron population were addressed. They found that these factors are significantly affected by the metal work function of the tip. Then they performed TERS and TEPL mappings of 1L MoS_2 using an Ag-coated probe and obtained an excellent spatial resolution of ~20 nm (Fig. 3a–d), which is 18 times better than that of the far field imaging in the same region and only 1/25 of the excitation laser wavelength. They also observed a quenching centre with a size of ~40 nm on 1L MoS_2 using TEPL. Their studies indicate that intrinsic defects may strongly mediate the local excitonic properties of 2D TMDs. This is also the first time that TERS and TEPL have been successfully used in the characterisation of 2D TMD materials.

1L TMD thin layers prepared by the CVD method contain a much higher density of defects than mechanically exfoliated samples.[56] These defects always cause more profound PL intensity variation inside a 1L flake. In 2017, Lee *et al.* imaged the exciton PL distribution of CVD prepared 1L WS_2 samples using near-field spectroscopy.[53] As shown in Fig. 3e–g, they found that the distribution of neutral excitons (A^0) is relatively uniform and is less affected by structural defects, but trions (A^-) and defect induced excitons (X^D) are strongly affected by structural defects. It was proposed that these profound distributions of A^0, A^- and X^D excitons are strongly dependent on the distribution of defects generated during sample preparation. In another TERS and TEPL study of CVD-grown MoS_2 flakes, Okuno *et al.* successfully observed the transformation steps from 1L to a bilayer (2L). The local PL of defects at the edges of 1L MoS_2 was also observed.[57] During the growth of

 This journal is © The Royal Society of Chemistry 2022

Published on 17 November 2022. Downloaded by Yunnan University on 8/14/2025 5:32:42 PM.

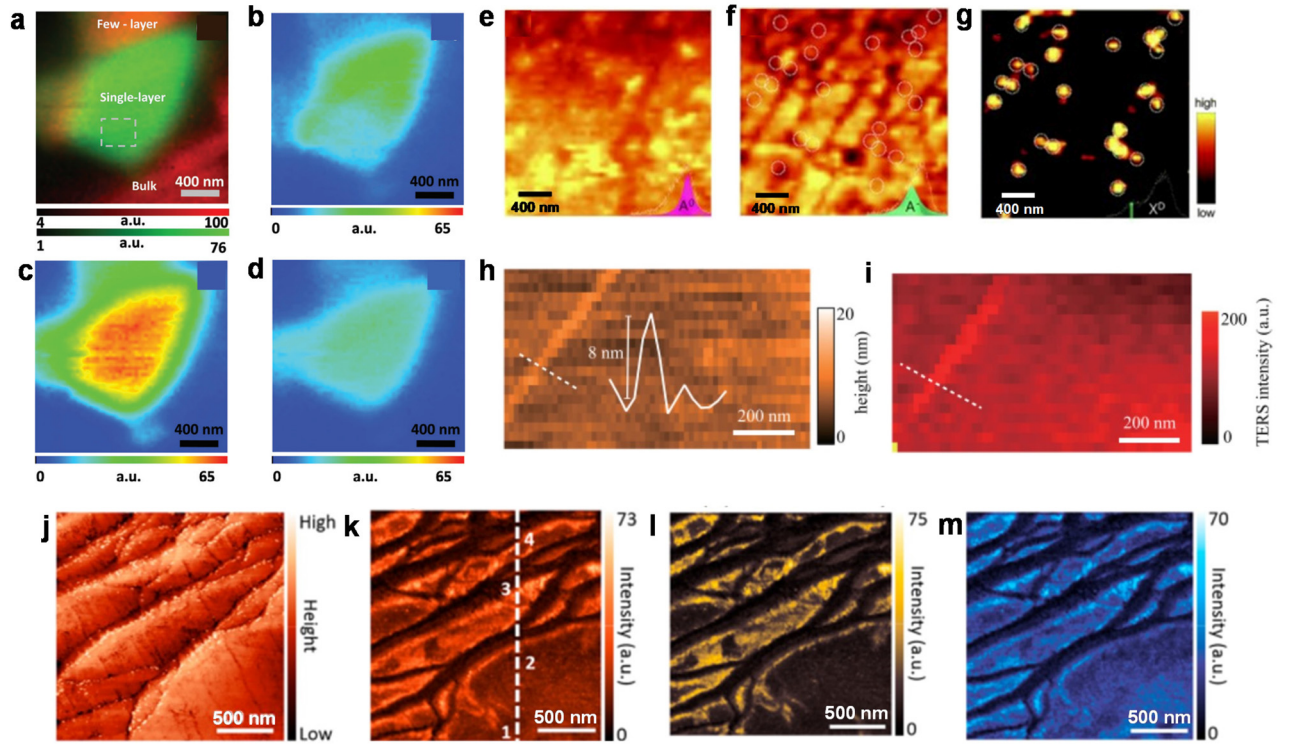

Fig. 3 (a) Overlay image of the TERS image obtained using the A_{1g} Raman band intensity (red) and the TEPL image obtained using the A^- exciton band intensity (green); A^0 exciton (b), trion (c) and B exciton (d) PL intensity images deconvoluted from the PL spectra measured at each pixel in the near-field of an Ag-coated tip;[25] near-field PL images of the A^0 excitons (e), trions (f), and local defect excitons (g) of 1L WS_2;[53] AFM height (h) and TERS (i) images of a MoS_2 sample and the corresponding height line profile along the white dotted line;[54] multispectral TERS images of defective 1L WS_2, STM height (j), Raman intensity images of A_{1g} (k), 2LA(M) (l) and defect peaks (m).[19] (a–d) have been adapted/reproduced from ref. 25 with permission from the Royal Society of Chemistry, copyright 2016; (e–g) have been adapted/reproduced from ref. 53 with permission from the Royal Society of Chemistry, copyright 2017; (h and i) have been adapted/reproduced from ref. 54 with permission from AIP publishing, copyright 2019; and (j–m) have been adapted/reproduced from ref. 19 with permission from the American Chemistry Society, copyright 2018.

2D TMDs, heterogeneous defects in the nanometre scale are always produced, which induce distinguishable Raman features. Lee *et al.* first performed tip-enhanced nanoscopy of these defects of WS_2 using TERS and found different TERS signals which originate from two majority defects, *i.e.*, S- and W-vacancies.[58] In another study, Kato *et al.* developed a modified tip-enhanced nanoscopy system with the capability of stabilizing an image for a long time as several hours. They successfully found nanoscale defects in large size WS_2 (several microns) using a defect related TERS peak at 410 cm^{-1}. The defect density was estimated to be 5.2%.[59]

Wrinkles might be formed in 2D TMD thin layers prepared by mechanical exfoliation or transferring. The strain field may change the elastic properties of the surrounding area, inducing Raman signal variation in the nanoscale spatial width around the wrinkles. Kato *et al.* conducted TERS mapping of a wrinkle on 1L MoS_2 and obtained a spatial resolution of 20 nm (Fig. 3h and i).[54] In an AFM topography image, a protrusion with a height of 8 nm (Fig. 3h) was assigned to a wrinkle on the 1L MoS_2. Benefiting from the high resolution of TERS, they successfully captured a high resolution nanoscopy image of this wrinkle, which gives a stronger A_{1g} peak intensity than the basal plane of 1L MoS_2. The shape of this wrinkle measured by TERS imaging agrees well with the topography image obtained from AFM.

For TMD thin layers deposited on a corrugate surface, it is expected that even higher density of defects existing due to the unwanted lattice merging of multiple nanocrystals during the growth process. Lee *et al.* studied the defects of 1L WS_2 deposited on a gold thin film with TERS and obtained an enhancement factor of 2.7×10^4 and a spatial resolution of 45 nm (Fig. 3j–m).[19] They found that both the A_{1g} and 2LA(M) peaks of MoS_2 redshifted at the places where a high density of defects exists. Two new Raman peaks emerge at ~400 cm^{-1} and ~432 cm^{-1} can be attributed to defect-induced D and D′ modes. These two new peaks have not been seen in mechanically exfoliated or CVD deposited 1L WS_2 flakes on flat substrates. They speculated that this phenomenon is related to the density of sulphur atomic vacancy. Their DFT calculations indicate that the increasing density of sulphur atomic vacancy induces a red shift of the out-of-plane Raman modes. When the vacancy concentration is 15.625%, the A_{1g}, D and D′ peaks redshifted by 3.14 cm^{-1}, 10.27 cm^{-1} and 0.24 cm^{-1} respectively, which agree well with their experimental results.

The edge is another typical non-ideal structure in 2D TMD materials. The discontinuity of lattice periodicity at the edge of

Published on 17 November 2022. Downloaded by Yunnan University on 8/14/2025 5:32:42 PM.

a perfect TMD lattice generates defect related mid-gap states.[60] The phonon and exciton behaviours at the edge are expected to be modulated by these defect states. Moreover, the diffusion of chalcogenide atoms during the CVD growth is expected to emerge at the edges, which causes higher density of defects than the inner part of a TMD flake and induces a much stronger modulation of the PL nonhomogeneity over a TMD flake.[61] Driguez *et al.* conducted TEPL measurement on a MoS_2 flake using a non-gap nanoscopy system.[62] They found that the PL intensity and energy at the edge are much larger than those in interior region (Fig. 4a–d). This could be attributed to the high density of structural defects introduced in the growth of MoS_2 edge, resulting in a higher density of A^0 excitons than trions. Therefore, the PL peak shifts to the high energy side, meanwhile the PL intensity increases accordingly. Huang *et al.* successfully conducted a TERS study of few-layer MoS_2 edges with a spatial resolution of 7 nm.[63] They found that the Raman peak at ~220 cm^{-1} can only be observed at the edges of 1L and 2L (Fig. 4e–h), while a Raman peak at ~396 cm^{-1} generated by the LA + TA vibrational mode can only be found at the transition step between 1L and 2L MoS_2. The LA + TA Raman peak originates from the bending of the energy band, which was further used to characterise the energy band bending region at the step of 2L MoS_2 with a spatial resolution better than 7 nm. As shown in Fig. 4h, they found that the A_{1g} peak red shifted (blue shifted) at the zigzag (armchair) edges, which could be attributed to the different strains generated by different edge structures. Therefore, they proposed that this can be used to judge whether the MoS_2 edge is zigzag or armchair.

The grain boundary (GB) is another typical defect that formed by two flakes merging at a certain angle. The dislocations at GBs usually generate deep gap states and strongly affect the electron and exciton diffusions in 2D TMDs.[64,65] Su *et al.* used a tip-enhanced nanoscopy method to investigate the optoelectronic behaviour of GBs in 1L WSe_2 (Fig. 4j and k). They found that the excitonic PL quenching at the GBs depends significantly on the tilting angle of two 1L flakes.[28] Further study indicates that the work function and charge accumulation are all strongly dependent on the tilting angles and can be correlated with the dislocation type. However, the geometric size of dislocations at GBs is only ~1 nm. Spatially identifying the optical influence of dislocations needs a nanoscopic tool with Angstrom spatial resolution. Recent studies showed that TERS operated at liquid helium temperature was

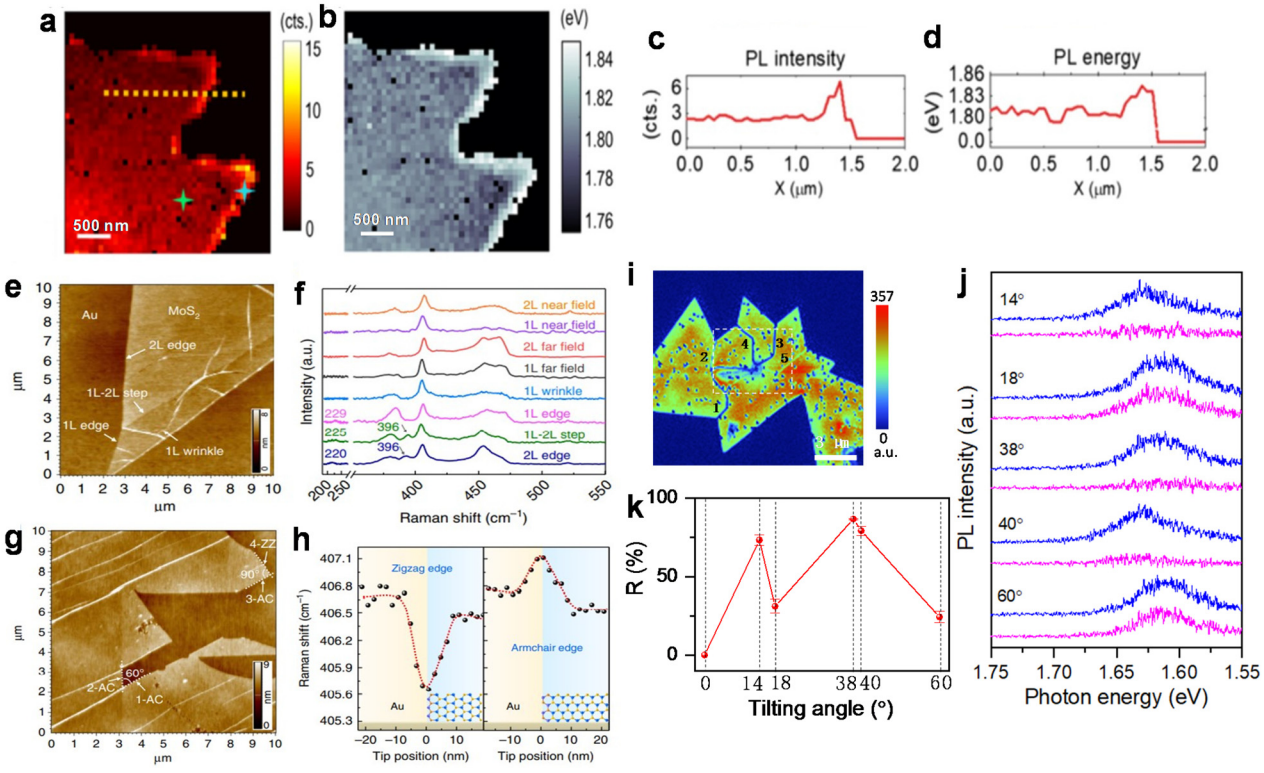

Fig. 4 TEPL intensity (a) and energy (b) of 1L MoS_2 prepared by CVD; PL intensity (c) and energy (d) profiles along the dashed line in (a); AFM topography image (e) of mechanically exfoliated MoS_2 with different types of 1D defects on an Au substrate and (f) TERS spectra of four 1D defects and the basal plane in MoS_2; AFM topography image (g) of mechanically exfoliated 1L MoS_2 with different edge angles on an Au substrate and a plot of then peak position (h) when the tip obtained through the armchair and zigzag edges, respectively (lower panel);[63] TEPL mapping of grain boundaries with different tilting angles (i); and tilting angle dependence of PL spectra (j) and quenching ratio R (k) in the grain boundaries of 1L WSe_2.[28] (a–d) have been adapted/reproduced from ref. 62 with permission John Wiley and Sons, copyright 2019; (e–h) have been adapted/reproduced from ref. 63 with permission from Springer Nature, copyright 2019; and (i–k) have been adapted/reproduced from ref. 28 with permission from the American Chemistry Society, copyright 2021.

This journal is © The Royal Society of Chemistry 2022

Published on 17 November 2022. Downloaded by Yunnan University on 8/14/2025 5:32:42 PM.

able to provide vibration information of a single sheet of silicene with a spatial resolution better than 1 nm.[66] This indicates that low temperature TERS or TEPL can be potentially used to identify the electron and exciton behaviours in a nanoscale region neighbouring a single dislocation.

Very recently, Jelken *et al.* used TERS combined with lateral force and peakforce mode AFM to unveil a hidden flower-like structure of WS_2. Their work shows that the tip-enhanced nanoscopy and nanomechanical combined method is a reliable and promising approach to unveil structural features in 2D TMD thin layers that cannot be measured by AFM topography scans.[67]

Applications of tip-enhanced nanoscopy in the characterisation of strain in 2D TMD thin layers

In addition to the defects generated in sample preparation, strain accumulation is usually seen in transferred TMD thin layers. In the CVD procedure, the cooling of samples from hundreds of Celsius degrees to ambient temperature causes residue thermal strain in the obtained samples.[68] Such unintentionally introduced strain is spatially accumulated and usually modifies the local band structure,[69] resulting in the localised optoelectronic properties of TMD thin layers. In a reverse view, local strain can also be rationally utilized to generate nanostructures of TMDs with different optoelectronic properties.[70] Recently, TERS and TEPL had been employed to study the influence of intentionally introduced local strain to TMD thin layers. Milekhin *et al.* placed 1L MoS_2 onto periodically arranged Au nanopillars and studied it with TERS (shown in Fig. 5a and b). They found that the Raman intensities of the different phonon modes of 1L MoS_2 were greatly enhanced, which can be attributed to the plasmonic gap between the Au tip apex and the Au nanoclusters. They also observed a crystal structure transition of MoS_2 from the 2H to 1T phase at the pillar edges.[71]

In another study, Rahaman *et al.* prepared periodic gold nanotriangles using nanosphere lithography, and then they transferred trilayer MoS_2 onto these nanostructures (shown in Fig. 5c).[72] The MoS_2 area at the edge of gold nanotriangles is strongly affected by strain, while the flat area in the centre is free of strain. As a consequence, there is an obvious difference of the Raman signals collected from the central flat area and the edge of gold nanotriangles (Fig. 5d). The second derivative of the AFM topography image is presented in Fig. 5e. In this image, the higher the brightness, the greater the bending and the larger the strain. TERS mapping was performed in the area corresponding to Fig. 5c, shown by a TERS intensity image in Fig. 5f. The spatial resolution of the TERS map was determined to be better than 25 nm by fitting the differential curve of an intensity profile in the TERS image (Fig. 5g). The peak positions of the E_{2g} and A_{1g} modes of 10 points with different levels of strain (in Fig. 5e) are plotted in Fig. 5h. They found that the shifts of the two first-order Raman peaks increase with increasing strain.

Zhang *et al.* successfully used TERS and TEPL to study the local strain in 1L MoS_2.[70] They first deposited 1L MoS_2 onto gold pyramids, inducing different local strains. TERS and TEPL line scans were carried out across the edge of a gold pyramid. In the obtained results, it was found that with the increasing strain, the E_{2g} and A_{1g} peaks of MoS_2 redshifted. They proposed

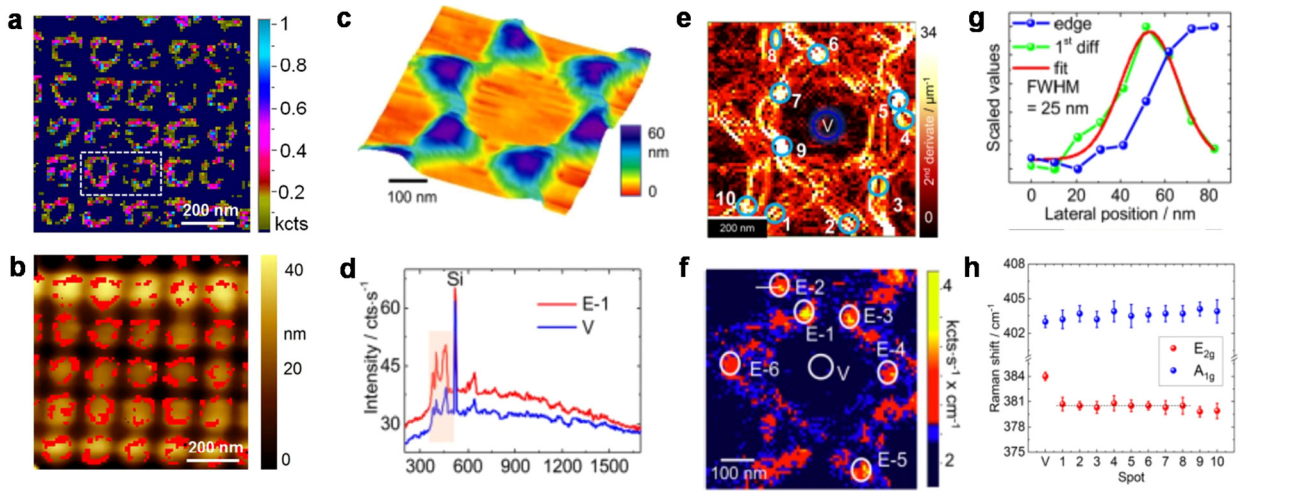

Fig. 5 (a) Raman intensity image of A_{1g} mode; (b) overlay image using the TERS intensity image in a and the simultaneously measured AFM topography image;[71] (c) AFM topography of an interesting area during TERS imaging; (d) the averaged TERS spectra of the two different areas noted in the TERS intensity image; (e) the second order derivative (SOD) of AFM topography; (f) TERS intensity image of MoS_2 acquired in the spectral range from 360 to 480 cm^{-1}; (g) the intensity profile of the cross section along the white solid line in the TERS image and the fitting to determine the spatial resolution; and (h) the fitted peak position of the corresponding spots in the SOD image (e).[72] (a and b) have been adapted/reproduced from ref. 71 with permission from the Royal Society of Chemistry, copyright 2018 and (c–h) have been adapted/reproduced from ref. 72 with permission from the American Chemistry Society, copyright 2017.

Published on 17 November 2022. Downloaded by Yunnan University on 8/14/2025 5:32:42 PM.

that this change can be attributed to the modification of the energy band structure and phonon dispersion relationship of 1L MoS_2 under tensile strain. Koo *et al.* used TEPL to study the strain induced band structure modification of 1L MoS_2 on a SiO_2 substrate. They found that the PL peak at a fold of MoS_2 red shifted compared with that at the flat area, which is due to the lowered conduction band minimum induced by tensile strain. Furthermore, an Au tip was used to apply compressive strain to the folded area. They found that the PL peak blue shifted with increasing strain. This change is elastic, *i.e.*, after releasing the compressive strain, the PL peak restores to its original position.[73] This strategy could be potentially used to design logical units applied in nanoscale optoelectronic devices.

In 2019, Carmesin *et al.* studied the strain induced modulation of the optoelectronic properties of 1L MoS_2 nanobubbles through TEPL characterisation. The influence of local strain on the MoS_2 energy band was investigated by testing multiple points on the nanobubbles,[74] shown in Fig. 6a and b. They found that the nonuniform strain forms a pocket, and the energy band in this strain pocket is highly localised. Meanwhile, the carrier limitation caused by local changes of the dielectric environment needs to be considered. They further showed that these two effects are crucial for changing the local electronic states and optical properties of MoS_2. In 2020, Darlington *et al.* used TEPL to characterise 1L WSe_2 and studied the strain induced exciton localization in the nanobubbles. They found that these localised excitons generally lead to a circular low-energy distribution around the high-energy centre of the bubble. Their experiment established robust experimental and theoretical connections for the strain induced formation of quantum dot states in 1L TMD semiconductors for the first time. Their results show that the LX states retain localised at room temperature. Their studies indicated that tip-enhanced nanoscopy has remarkable potential applications in strain engineering of optoelectronic and quantum optical architectures.[75] Recently, Rodriguez *et al.* used low frequency TERS mapping to study a WS_2/WSe_2 heterostructure bubble (Fig. 6c–e). Owing to a spatial resolution ~10 nm, a heterostructure bubble with a size of ~50 nm, which is totally invisible in far field Raman imaging, can be clearly seen in the TERS intensity image generated using low frequency Raman mode at ~22 cm^{-1}. The decoupling of WS_2 and WSe_2 layers marked by the disappearance of the low frequency interlayer phonon mode was also observed by TERS.[76]

A TERS probe can also be used as an intermedium to load controllable strain onto TMD thin layers. As shown in Fig. 7a–c.

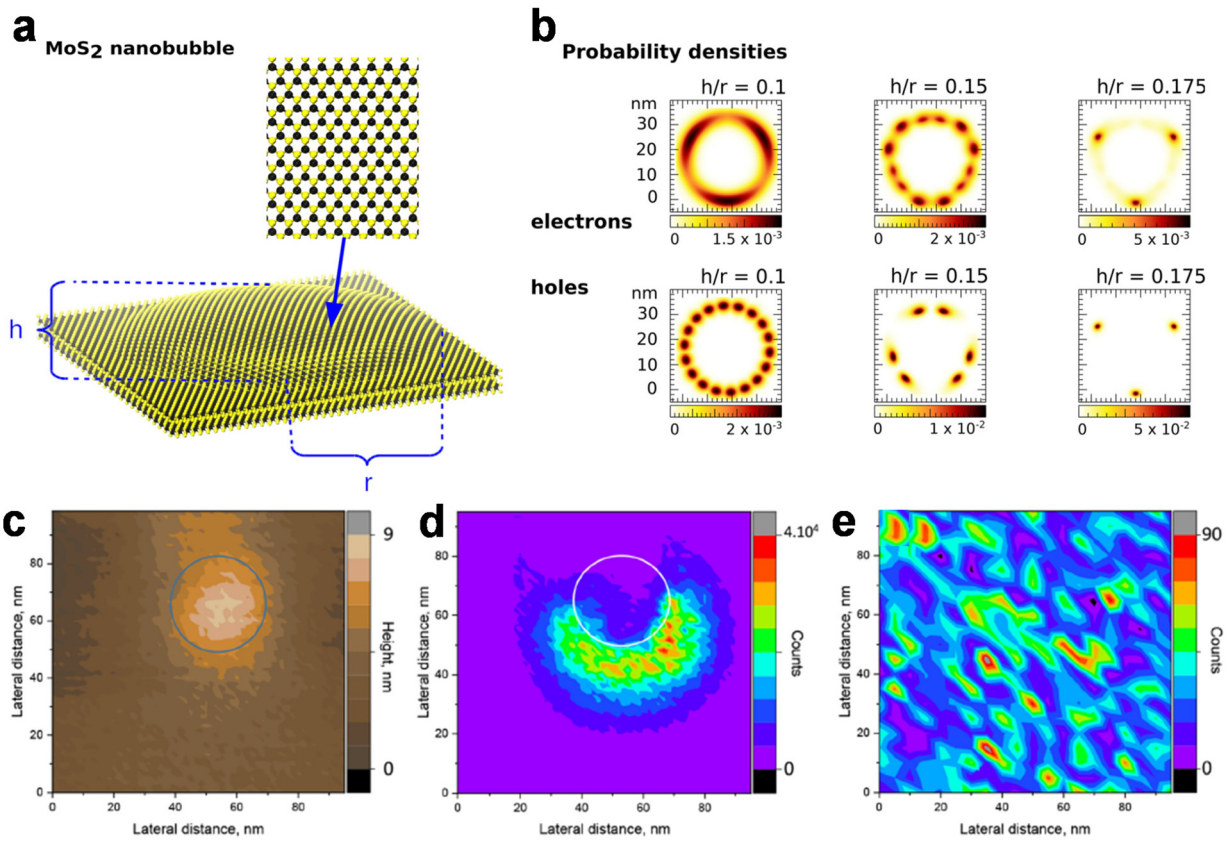

Fig. 6 (a) A MoS_2 air nanobubble with radius r and height h; (b) top view of the probability densities for electrons and holes at bubbles with different h/r ratios;[74] (c) AFM topography image of a WS_2/WSe_2 bubble; (d)low frequency TERS and (e) far field images of the bubble in (c) using Raman mode at 22 cm^{-1}.[76] (a and b) have been adapted/reproduced from ref. 74 with permission from the American Chemistry Society, copyright 2019 and (c–e) have been adapted/reproduced from ref. 76 with permission from the American Chemistry Society, copyright 2022.

 This journal is © The Royal Society of Chemistry 2022

Published on 17 November 2022. Downloaded by Yunnan University on 8/14/2025 5:32:42 PM.

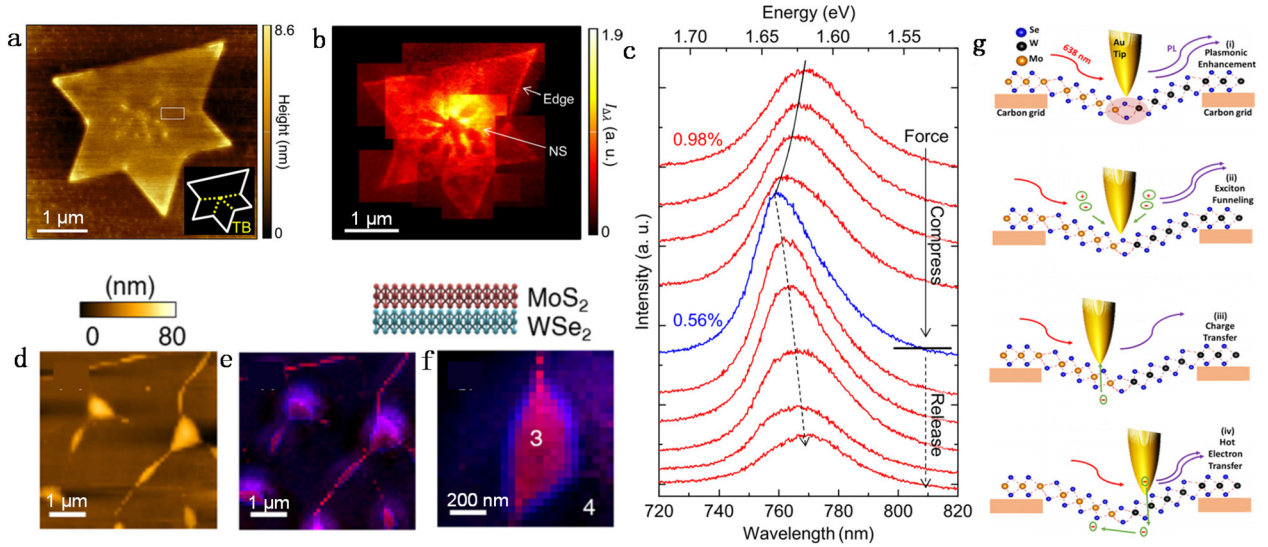

Fig. 7 AFM (a) and TEPL (b) images of a 1L WSe_2 flake with different heterogeneities; (c) reversible evolution of TEPL spectra under the modest nanomechanical tip–sample force interaction;[21] AFM topography (d) and TEPL intensity (e and f) images of the nanobubbles on MoS_2/WSe_2 heterostructures; and (g) schematics of the PL enhancement mechanisms of TEPL on a freestanding $WSe_2/MoSe_2$ heterostructure.[74] (a–c) have been adapted/reproduced ref. 21 with permission from American Chemistry Society, copyright 2016 and (d–g) have been adapted/reproduced from ref. 74 with permission from IOP Publishing, Ltd, copyright 2019.

Park *et al.* used TERS and TEPL to study the strain induced excitonic PL variation in 1L WSe_2.[21] They used an active Au metallic probe to control the applied strain at the nanoscale and tune the local bandgap reversibly. Then they studied the effects of strain and defect on PL at different structural heterogeneities. Rodriguez *et al.* found there are new PL peaks near the PL energy of the intralayer excitons of a MoS_2/WSe_2 heterostructure.[77] They believed that these peaks are caused by the influence of micro strain in blisters and nanobubbles. Through TERS and TEPL (Fig. 7d–f), they proved that even a bubble with a size of only 60 nm can produce such PL peaks.

Albagami *et al.* used TEPL to the characterise freestanding nanobubbles of TMD thin layers.[78] They observed a PL signal change in the nanobubbles and studied the competition between the PL enhancement mechanisms and nanoindentation as a function of the tip–sample distance (Fig. 7g). They believed that the difference observed in the experiment may be caused by many factors, such as the competition between quantum plasma suppression, strain induced exciton funnel enhancement of the PL signal, charge transfer from $MoSe_2$ to a gold tip, quantum plasma hot electron transfer from the gold tip to a $WSe_2/MoSe_2$ junction, *etc.*

Nanoscopy of TMD HJs

In addition to local defects and strain in 2D TMDs materials, TERS and TEPL can also be used to investigate the HJs of 2D TMDs. A clear junction interface without atomic interdiffusion is desirable for an abrupt junction. However, at the HJ interface of CVD grown samples, an alloyed transition region is often formed due to atomic interdiffusion. The nanoscopy study of HJs is initialized by imaging the junction interface using TERS and TEPL. Liu *et al.* conducted TEPL measurements on a MoS_2/WS_2 lateral HJ.[79] Owing to the good spatial resolution of TEPL, they can identify the MoS_2 and WS_2 junction interface that cannot be clearly distinguished using far field PL imaging. Sahoo *et al.* studied a $WSe_2/MoSe_2$ lateral HJ using TERS. A sharp junction interface with negligible interdiffusion was observed.[80] Xue *et al.* performed TEPL to characterise a 1L $MoSe_2/WSe_2$ lateral HJ. With a spatial resolution of ~40 nm, they obtained a clear interface of the HJ.[30]

Shao *et al.* studied abrupt and graded MoS_2/WS_2 lateral HJs using TERS and TEPL.[81] Combining the far field Raman and PL spectra and AFM image of this region, it can be concluded that these two lateral HJs are composed of 2L WS_2 and MoS_2. Then they conducted TERS and TEPL on these two HJs and obtained a spatial resolution better than 40 nm (Fig. 8a–d). As for abrupt HJs, the MoS_2-like 2LA(M), WS_2-like A_{1g}, exciton PL intensities and energies of MoS_2 and WS_2 exhibit abrupt transitions at the junction interface within a spatial width of a single pixel. For a graded junction, the WS_2 and MoS_2 areas can also be easily distinguished in TERS and TEPL intensity images. However, a low Raman and PL intensity area assigned to an alloyed area with a spatial width of 300–700 nm is sandwiched between the MoS_2 and WS_2 areas. No clear junction interface can be identified. They estimated the stoichiometry in the nanoscale vicinity of the junction interface using the Raman peak intensity (Fig. 8e and f). They combined these data and obtained the diffusion coefficient of W in MoS_2 as $0.54 \pm 0.18 \times 10^{-12}$ cm^2 s^{-1}. The obtained results indicate that TEPL and TERS could be further used to deeply understand the composition of the HJs at the nanoscale.

Similar alloyed regions of TMD HJs were observed by Garg *et al.* using TERS.[82] The CPD image of a 1L MoS_2/WS_2 lateral heterostructure is presented in Fig. 8g. Typical Raman spectra

Published on 17 November 2022. Downloaded by Yunnan University on 8/14/2025 5:32:42 PM.

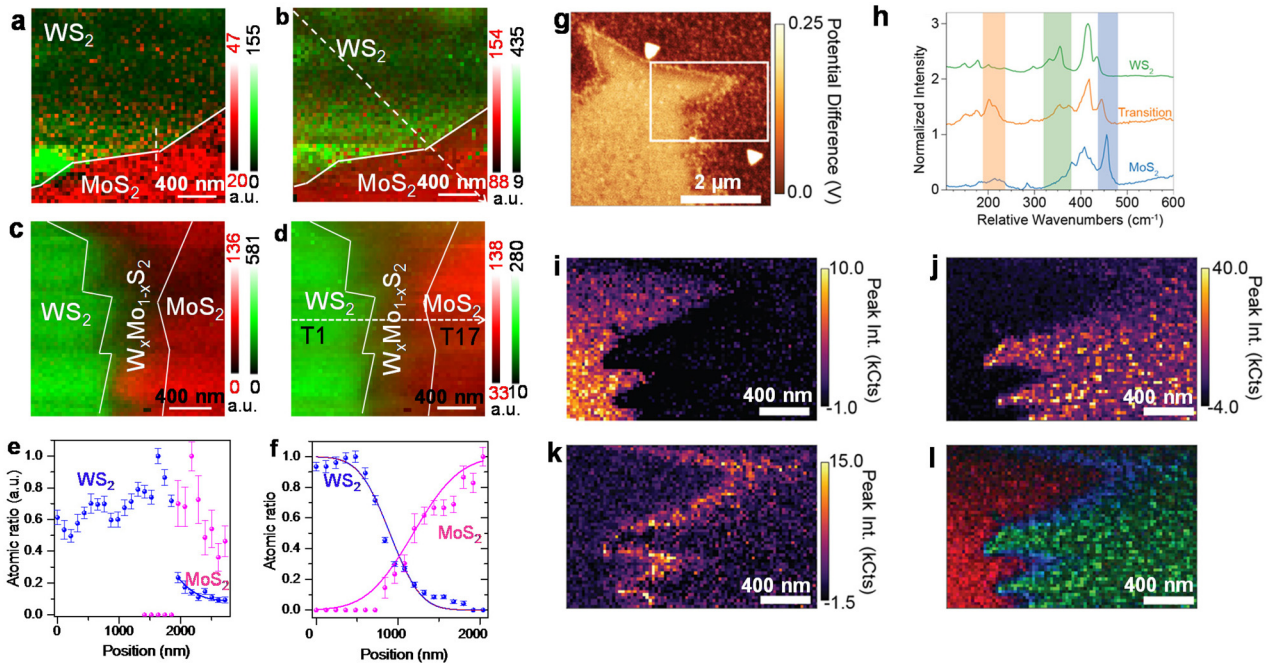

Fig. 8 (a) Overlay TERS intensity image of an abrupt HJ using the A_{1g} peak of WS_2 (green) and the 2LA(M) of MoS_2 (red); (b) overlay TEPL intensity image of an abrupt HJ using the A excitons of WS_2 (green) and MoS_2 (red); (c) TERS intensity image of a graded HJ using the A_{1g} peak of WS_2 (green) and 2LA(M) of MoS_2 (red); (d) overlay TEPL intensity image of a graded HJ using the *A* excitons of WS_2 (green) and MoS_2 (red); (e and f) atomic ratio of W and Mo across abrupt and graded HJs, respectively; (g) CPD image of the region characterised with TERS;[81] (h) representative semi-resonant TERS spectra of the 1L MoS_2 core, 1L WS_2 shell, and the transition regions of a 1L MoS_2/WS_2 lateral heterostructure; (i) spatial image of the peak intensity in the 440–480 cm^{-1} band of 1L MoS_2; (j) spatial image of the peak intensity in the 320–380 cm^{-1} band of the 1L WS_2 shell; (k) spatial image of the peak intensity in the 190–230 cm^{-1} resonant band associated with the alloyed transition region; and (l) combined image of the TERS bands with the 1L MoS_2 band (red channel), the alloyed transition band (blue channel), and the 1L WS_2 band (green channel).[82] (a–f) have been adapted/reproduced from ref. 81 with permission from the American Chemistry Society, copyright 2021 and (g–i) have been adapted/reproduced from ref. 82 with permission from American Chemistry Society, copyright 2021.

collected at the interface show characteristics of MoS_2 and WS_2, indicating an alloyed layer at the interface (Fig. 8h). They used TERS to investigate the interface of this lateral HJ and obtained a spatial resolution of ~50 nm. They found that the intensities of the ~200 and ~215 cm^{-1} Raman modes are substantially higher in the transition region. From the TERS intensity images obtained using these peaks (Fig. 8i–l), a clear transition region of this lateral HJ can be seen. The spatial width variation of the transition region separating the core and shell of this HJ was also obtained. Then they conducted non-resonant TERS in the same region. They found that the peak of A′ (Γ) mode red shifted from 455 cm^{-1} of the 1L MoS_2 core to 435 cm^{-1} of the 1L WS_2 shell. In the transition region, a new mode bridging these two modes appear at 442 cm^{-1}, which can be used to characterise the transition region.

In addition to the lateral HJs, vertical HJs had also been investigated by TERS. Krayev *et al.* studied the vertical HJs of WS_2/WSe_2 using TERS operated with multiple excitation laser wavelengths of 638, 671 and 785 nm. Owing to the different resonance of WS_2 and WSe_2 with the excitation laser wavelength, WS_2 shows a strong enhancement at three wavelengths, while WSe_2 is quite insensitive to the 638 nm laser. Combined with the CPD obtained from the KPFM scan, the vertical HJ areas can be unambiguously distinguished.[83]

In addition to the aforementioned progress of HJs, there are still a handful of unsolved issues challenging the multifunctionality of the nanoscopic method. For example, local strain at the semiconductor HJ interface induced by the lattice mismatch and growth parameters strongly modulates the local electronic band structure. The study of this effect preliminarily requires a high quality HJ sample with a sharp and clear interface to avoid the interference of the alloying effect. A highly sensitive TERS measurement is required to obtain the strain field at the junction interface by analysing the Raman peak shift. Then a TEPL scan is required to obtain the local exciton energy shift induced by the strain. A further correlation between the local energy band modification and the strain needs to be addressed.

Applications of tip-enhanced nanoscopy combined with electrical SPM at the nanoscale

Recently, TERS and TEPL had been combined with electric SPM, such as Kelvin probe force microscopy (KPFM), scanning capacitance microscopy, *etc.*, and spatially identifying defect

 This journal is © The Royal Society of Chemistry 2022

Published on 17 November 2022. Downloaded by Yunnan University on 8/14/2025 5:32:42 PM.

related physical properties at the nanoscale were achieved, providing a novel analytical tool to study the optoelectronic and electrical properties of 2D TMD materials. Jariwala *et al.* used a TERS and KPFM combined method to investigate multilayer WSe_2 flakes.[85] As shown in Fig. 9, the TERS intensity (in the range of 220–280 cm^{-1}) image corresponds very well with AFM topography and CPD images (Fig. 9a–c). Representative TERS spectra collected from the high and low CPD areas are shown in Fig. 9d. The distribution of the TERS intensity associated with multiple resonant peaks in the range of 220–280 cm^{-1} correlates well with the distribution of domains exhibiting high CPD. On the other hand, non-resonant TERS spectra are obtained in the area with lower CPD. Then they conducted a series of experiments to determine whether the correlation between the surface potential and the resonant-enhanced Raman spectrum is due to the underlying metal or an intrinsic feature of WSe_2 samples. The experimental results suggest that the observed non-uniformities arise from crystalline intrinsic variations in WSe_2. Their research indicates the potential applications of the TERS and KPFM combined method in the characterisation of the nanoheterogeneities of 2D TMDs.

Yao *et al.* studied the defect induced localised optoelectronic properties of 1L WS_2 by combining TEPL with *in situ* photosensitive KPFM.[28] They first studied the correlation of defect distribution with CPD distribution and then studied the distribution of excitons (Fig. 9e and f). They took six points "T1"–"T6" at areas with different defects (shown in Fig. 9g–i) and further found that these areas give different TEPL intensity ratios of A^0 and A^- excitons. They proposed that this is possibly due to the higher density of single sulphur and W-3S vacancies in the edge region of 1L WS_2 than in the interior part. In addition, they found two categories of low CPD lines in Fig. 9j and k. At the first category ("I"), the PL intensities of both A^0 and A^- excitons are quenched. However, in the second category ("II"), the PL intensities of both A^0 and A^- excitons are enhanced. They proposed that such a PL enhancement or quenching of A^0 and A^- excitons strongly depends on the radiative recombination rate of neutral excitons (Γ_{A^0}) and trions (Γ_{A^-}) and also the transition rate from the neutral excitons to trions (k). Their method enables direct correlation of localised optoelectronic properties with defect distributions at the nanoscale.

TEPL was also combined with KPFM to study the dynamic control of the local exciton recombination process. He *et al.* used the TEPL and KPFM combined method to achieve a high resolution TEPL mapping of the WS_2 surface and realized the modulation of excitons by controlling the distance between the plasmonic tip and the sample surface.[84] As shown in Fig. 10a–d, there are two representative tip–sample coupling regimes as a function of the tip–sample distance (d), *i.e.*, classical coupling (CC) and quantum coupling (QC). When d = 0.31 nm, the PL intensity ratio of X^- to X^0 excitons is larger than that at d = 1.03 nm, which indicates the role of tunnelling. Subsequently, they studied the relationship between the population change of X^0 and X^- excitons as a function of the tip–sample distance. They found that there are two conditions,

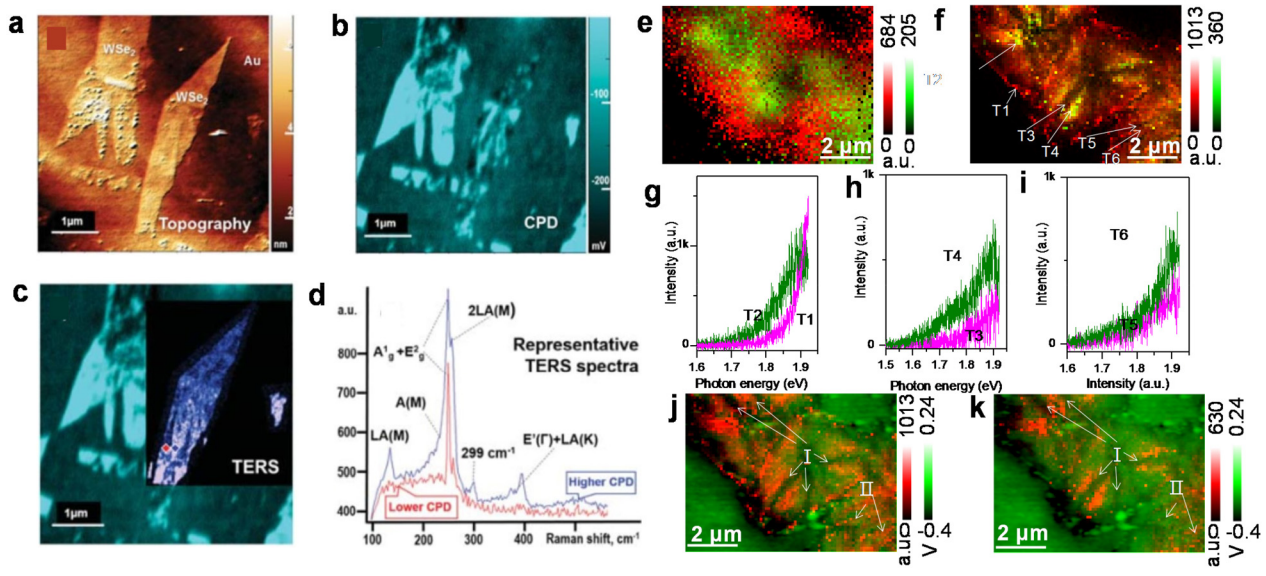

Fig. 9 (a) AFM topography image of multilayer WSe_2 exfoliated on template stripped gold; (b) surface potential image of the same area in image (a); (c) TERS intensity image of the complex A(M) + A_{1g} + E_{2g} + 2LA(M) peak on the background of surface potential; (d) averaged TERS spectra from adjacent areas with higher surface potential (blue spectrum, resonant behaviour) and lower surface potential (red spectrum, non-resonant behaviour);[85] overlay far field (e) and near field (f) PL images of neutral excitons (red) and defect-bounded excitons (green); (g) TEPL spectra from the high intensity of neutral excitons (T1) and the high intensity of trions (T2); (h) TEPL spectra from the line defect I (T3) and neighbouring the line defect I (T4); (i) TEPL spectra from the line defect II (T6) and neighbouring the line defect II (T5); and overlay images of neutral excitons (j) and trions (k) with CPD in the corresponding area.[28] (a–d) have been adapted/reproduced from ref. 85 with permission from IOP publishing, Ltd, copyright 2018 and (e–k) have been adapted/reproduced from ref. 28 with permission from the American Chemistry Society, copyright 2020.

Published on 17 November 2022. Downloaded by Yunnan University on 8/14/2025 5:32:42 PM.

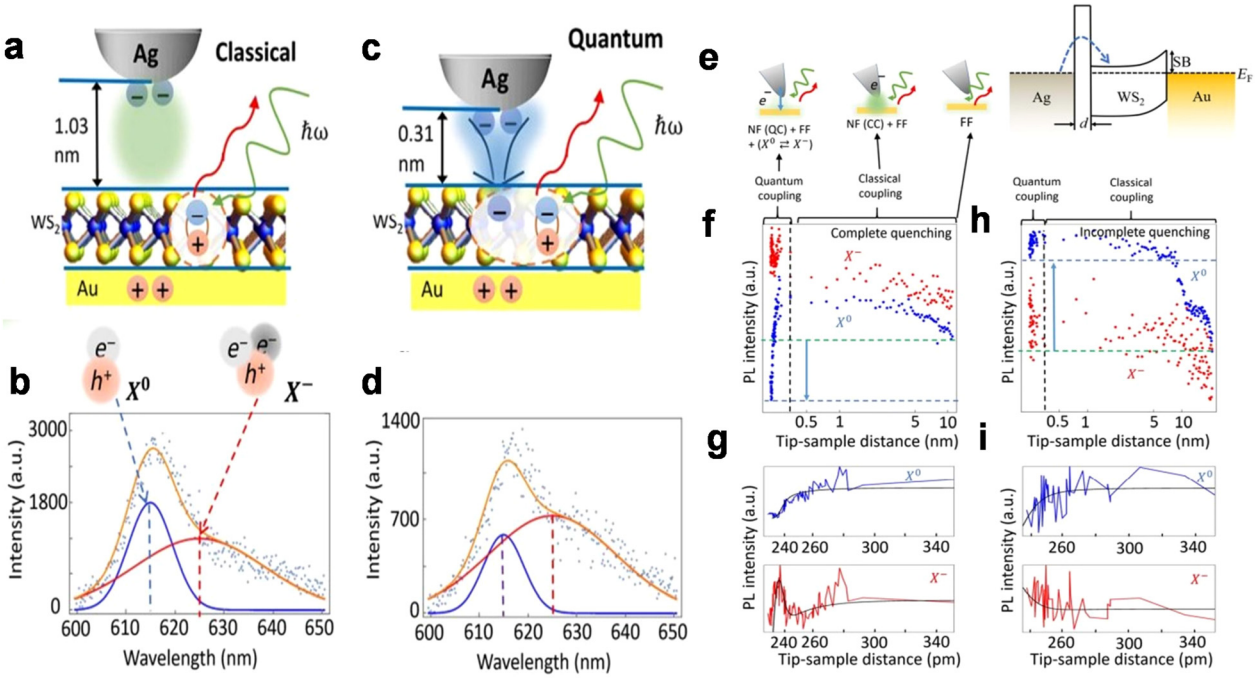

Fig. 10 (a) Schematic of the Au–Ag cavity with a tip–sample distance d > 1 nm that corresponds to the classical coupling (CC) regime; (b) PL spectra of X^0 and X^- in 1L WS_2 in the CC regime; (c and d) the corresponding sketch and PL spectra of 1L WS_2 in the Au–Ag picocavity in the quantum coupling (QC) regime with a tip–sample distance d < 0.35 nm; (e) energy diagram of the tip–sample–substrate (Ag–WS_2–Au) system with a Schottky barrier (SB); and (f–i) tip–sample distance dependence of the PL signal intensities of neutral excitons (X^0) and trions (X^-) in different situations.[84] This figure has been adapted/reproduced from ref. 84 with permission from the American Association for the Advancement of Science, copyright 2019.

i.e., the complete and incomplete PL quenching (Fig. 10e–i). They attributed this difference to the transition from X^0 to X^-.

The dynamic control of local excitons is also implemented in a $WSe_2/MoSe_2$ HJ by Tang *et al.*[86] It was found that when the tip–sample distance is less than 0.36 nm, the hot electrons generated by the tip will greatly enhance the PL intensity of the sample. There are a large number of holes in a 1L WSe_2 sample, which combines with the injected hot electrons to form excitons, resulting in an enhancement of the PL intensity. This effect is in a competitive relationship with the PL quenching effect caused by the tip electric field. Therefore, for 1L $MoSe_2$ with a low density of holes, the quenching effect caused by the tip electric field is dominant in this process. Then they repeated the experiments on a $WSe_2/MoSe_2$ HJ and found that the holes accumulated on the $MoSe_2$ side where the PL enhancement was seen. Their experiment points out that the carrier migration in HJs can be studied by accurately injecting hot electrons into HJs through TEPL, which provides a novel method for designing controllable nanoscale optoelectronic devices.

Conclusions

Based on the above discussions, a large number of studies and practices show that TERS and TEPL can be used as powerful analytical tools to study 2D TMDs. Owing to their excellent spatial resolution up to several nanometres, we can observe the primary defects, residue strain and alloying effects in TMDs at the nanoscale. In this work, we introduced the basic principle and configuration of TERS, and reviewed the progress of TERS and TEPL in the research of 2D TMDs in recent years. In addition to the reported data, TERS and TEPL still have great potential. In recent years, twist angle 2D materials have attracted the attention of researchers all over the world. The size of moiré superlattices in twisted angle 2D materials is often in the scale of nanometre, which has exceeded the spatial resolution of confocal Raman and PL spectroscopy. TERS and TEPL can satisfy this demand and help people to understand the atomic structure and local exciton properties in moiré supercells at the nanoscale. In the 2D TMD HJ, in addition to the alloying effect, there are still many factors that affect its properties, such as local strain, composition segregation and so on. These problems still need to be addressed, and TERS and TEPL will be powerful analytical tools. It is expected that TERS and TEPL will play important roles in the future research of TMD materials.

Author contributions

J.S: writing and formatting. W.S: writing, formatting and funding.

This journal is © The Royal Society of Chemistry 2022

Published on 17 November 2022. Downloaded by Yunnan University on 8/14/2025 5:32:42 PM.

Conflicts of interest

There are no conflicts to declare.

Acknowledgements

The authors acknowledge the financial support from the Zhejiang Provincial Natural Science Foundation of China (Grant No. LZ22A040003 and LY19E020012) and the Natural Science Foundation of China (Grant No. 52027809).

References

1 L. Su, Y. Yu, L. Cao and Y. Zhang, *Nano Res.*, 2015, **8**, 2686–2697.
2 A. Klein, S. Tiefenbacher, V. Eyert, C. Pettenkofer and W. Jaegermann, *Phys. Rev. B: Condens. Matter Mater. Phys.*, 2001, **64**, 205416.
3 B. Schuler, J.-H. Lee, C. Kastl, K. A. Cochrane, C. T. Chen, S. Refaely-Abramson, S. Yuan, E. van Veen, R. Roldán, N. J. Borys, R. J. Koch, S. Aloni, A. M. Schwartzberg, D. F. Ogletree, J. B. Neaton and A. Weber-Bargioni, *ACS Nano*, 2019, **13**, 10520–10534.
4 M. Precner, T. Polakovic, Q. Qiao, D. J. Trainer, A. V. Putilov, C. Di Giorgio, I. Cone, Y. Zhu, X. X. Xi, M. Iavarone and G. Karapetrov, *Sci. Rep.*, 2018, **8**, 6724.
5 A. M. van der Zande, P. Y. Huang, D. A. Chenet, T. C. Berkelbach, Y. You, G.-H. Lee, T. F. Heinz, D. R. Reichman, D. A. Muller and J. C. Hone, *Nat. Mater.*, 2013, **12**, 554–561.
6 B. Liu, M. Fathi, L. Chen, A. Abbas, Y. Ma and C. Zhou, *ACS Nano*, 2015, **9**, 6119–6127.
7 S. Najmaei, Z. Liu, W. Zhou, X. Zou, G. Shi, S. Lei, B. I. Yakobson, J.-C. Idrobo, P. M. Ajayan and J. Lou, *Nat. Mater.*, 2013, **12**, 754–759.
8 C. Huang, S. Wu, A. M. Sanchez, J. J. P. Peters, R. Beanland, J. S. Ross, P. Rivera, W. Yao, D. H. Cobden and X. Xu, *Nat. Mater.*, 2014, **13**, 1096–1101.
9 J. Shao, F. Chen, W. Su, N. Kumar, Y. Zeng, L. Wu and H.-W. Lu, *J. Phys. Chem. Lett.*, 2022, **13**, 3304–3309.
10 M.-Z. Qin, W.-X. Fu, H. Guo, C.-G. Niu, D.-W. Huang, C. Liang, Y.-Y. Yang, H.-Y. Liu, N. Tang and Q.-Q. Fan, *Adv. Colloid Interface Sci.*, 2021, **297**, 102540.
11 A. J. Goodman, D. H. Lien, G. H. Ahn, L. L. Spiegel, M. Amani, A. P. Willard, A. Javey and W. A. Tisdale, *J. Phys. Chem. C*, 2020, **124**, 12175–12184.
12 Y. Liu, R. Ghosh, D. Wu, A. Ismach, R. Ruoff and K. Lai, *Nano Lett.*, 2014, **14**, 4682–4686.
13 A. Azizi, X. Zou, P. Ercius, Z. Zhang, A. L. Elias, N. Perea-Lopez, G. Stone, M. Terrones, B. I. Yakobson and N. Alem, *Nat. Commun.*, 2014, **5**, 4867.
14 N. Kumar, S. Mignuzzi, W. Su and D. Roy, *EPJ Tech. Instrum.*, 2015, **2**, 9.
15 A. C. Gadelha, D. A. A. Ohlberg, C. Rabelo, E. G. S. Neto, T. L. Vasconcelos, J. L. Campos, J. S. Lemos, V. Ornelas, D. Miranda, R. Nadas, F. C. Santana, K. Watanabe, T. Taniguchi, B. van Troeye, M. Lamparski, V. Meunier, V.-H. Nguyen, D. Paszko, J.-C. Charlier, L. C. Campos, L. G. Cançado, G. Medeiros-Ribeiro and A. Jorio, *Nature*, 2021, **590**, 405–409.
16 Z. He, Z. Han, J. Yuan, A. M. Sinyukov, H. Eleuch, C. Niu, Z. Zhang, J. Lou, J. Hu, D. V. Voronine and M. O. Scully, *Sci. Adv.*, 2019, **5**, eaau8763.
17 T.-X. Huang, X. Cong, S.-S. Wu, K.-Q. Lin, X. Yao, Y.-H. He, J.-B. Wu, Y.-F. Bao, S.-C. Huang, X. Wang, P.-H. Tan and B. Ren, *Nat. Commun.*, 2019, **10**, 5544.
18 N. Kumar, S. Marchesini, T. Howe, L. Edwards, B. Brennan and A. J. Pollard, *J. Chem. Phys.*, 2020, **153**, 184708.
19 C. Lee, B. G. Jeong, S. J. Yun, Y. H. Lee, S. M. Lee and M. S. Jeong, *ACS Nano*, 2018, **12**, 9982–9990.
20 S. Mignuzzi, N. Kumar, B. Brennan, I. S. Gilmore, D. Richards, A. J. Pollard and D. Roy, *Nanoscale*, 2015, **7**, 19413–19418.
21 K.-D. Park, O. Khatib, V. Kravtsov, G. Clark, X. Xu and M. B. Raschke, *Nano Lett.*, 2016, **16**, 2621–2627.
22 W. Su, A. Esfandiar, O. Lancry, J. Shao, N. Kumar and M. Chaigneau, *Chem. Commun.*, 2021, **57**, 6895–6898.
23 W. Su, N. Kumar, N. Dai and D. Roy, *Chem. Commun.*, 2016, **52**, 8227–8230.
24 W. Su, N. Kumar, A. Krayev and M. Chaigneau, *Nat. Commun.*, 2018, **9**, 2891.
25 W. Su, N. Kumar, S. Mignuzzi, J. Crain and D. Roy, *Nanoscale*, 2016, **8**, 10564–10569.
26 W. Su, N. Kumar, H. Shu, O. Lancry and M. Chaigneau, *J. Phys. Chem. C*, 2021, **125**, 26883–26891.
27 W. Su, N. Kumar, S. J. Spencer, N. Dai and D. Roy, *Nano Res.*, 2015, **8**, 3878–3886.
28 Y. Yao, F. Chen, L. Fu, S. Ding, S. Zhao, Q. Zhang, W. Su, X. Ding and K. Song, *J. Phys. Chem. C*, 2020, **124**, 7591–7596.
29 C. Lee, S. T. Kim, B. G. Jeong, S. J. Yun, Y. J. Song, Y. H. Lee, D. J. Park and M. S. Jeong, *Sci. Rep.*, 2017, **7**, 40810.
30 W. Xue, P. K. Sahoo, J. Liu, H. Zong, X. Lai, S. Ambardar and D. V. Voronine, *J. Vac. Sci. Technol., A*, 2018, **36**, 05g502.
31 C. Tang, Z. He, W. Chen, S. Jia, J. Lou and D. V. Voronine, *Phys. Rev. B*, 2018, **98**, 041402.
32 P. K. Sahoo, H. Zong, J. Liu, W. Xue, X. Lai, H. R. Gutierrez and D. V. Voronine, *Opt. Mater. Express*, 2019, **9**, 1620–1631.
33 Y. Kim, S. J. Yun, E. Lee and J. Kim, *Opt. Mater. Express*, 2019, **9**, 1864–1871.
34 M. Asghari-Khiavi, B. R. Wood, P. Hojati-Talemi, A. Downes, D. McNaughton and A. Mechler, *J. Raman Spectrosc.*, 2012, **43**, 173–180.
35 C. F. Bohren and H. D, *Absorption and Scattering of Light by Small Particles*, Wiley, New York, 1983.
36 M. Q. Zhang, R. Wang, Z. D. Zhu, J. Wang and Q. Tian, *J. Opt.*, 2013, **15**, 055006.

Published on 17 November 2022. Downloaded by Yunnan University on 8/14/2025 5:32:42 PM.

37 R. E. Larsen and H. Metiu, *J. Chem. Phys.*, 2001, **114**, 6851–6860.
38 L. Novotny, R. X. Bian and X. S. Xie, *Phys. Rev. Lett.*, 1997, **79**, 645–648.
39 B. Pettinger, B. Ren, G. Picardi, R. Schuster and G. Ertl, *Phys. Rev. Lett.*, 2004, **92**, 096101.
40 S. Kawata, *Tip Enhancement*, Elsevier, Oxford, 2007.
41 N. Kumar, A. Rae and D. Roy, *Appl. Phys. Lett.*, 2014, **104**, 123106.
42 K. F. Mak, C. Lee, J. Hone, J. Shan and T. F. Heinz, *Phys. Rev. Lett.*, 2010, **105**, 136805.
43 L. Meng, Z. Yang, J. Chen and M. Sun, *Sci. Rep.*, 2015, **5**, 9240.
44 K.-D. Park, M. A. May, H. Leng, J. Wang, J. A. Kropp, T. Gougousi, M. Pelton and M. B. Raschke, *Sci. Adv.*, 2019, **5**, eaav5931.
45 R. Zhang, Y. Zhang, Z. C. Dong, S. Jiang, C. Zhang, L. G. Chen, L. Zhang, Y. Liao, J. Aizpurua, Y. Luo, J. L. Yang and J. G. Hou, *Nature*, 2013, **498**, 82–86.
46 J. Stadler, T. Schmid and R. Zenobi, *Nano Lett.*, 2010, **10**, 4514–4520.
47 P. J. Wang, D. Zhang, L. L. Li, Z. P. Li, L. S. Zhang and Y. Fang, *Plasmonics*, 2012, **7**, 555–561.
48 N. Kumar, B. M. Weckhuysen, A. J. Wain and A. J. Pollard, *Nat. Protoc.*, 2019, **14**, 1169–1193.
49 M. Sackrow, C. Stanciu, M. A. Lieb and A. J. Meixner, *ChemPhysChem*, 2008, **9**, 316–320.
50 J. Steidtner and B. Pettinger, *Phys. Rev. Lett.*, 2008, **100**, 236101.
51 A. Castellanos-Gomez, R. Roldán, E. Cappelluti, M. Buscema, F. Guinea, H. S. J. van der Zant and G. A. Steele, *Nano Lett.*, 2013, **13**, 5361–5366.
52 P. Cheng, Q. Zhou, X. Hu, S. Su, X. Wang, M. Jin, L. Shui, X. Gao, Y. Guan, R. Nözel, G. Zhou, Z. Zhang and J. Liu, *ACS Appl. Mater. Interfaces*, 2018, **10**, 23444–23450.
53 Y. Lee, S. J. Yun, Y. Kim, M. S. Kim, G. H. Han, A. K. Sood and J. Kim, *Nanoscale*, 2017, **9**, 2272–2278.
54 R. Kato, T. Umakoshi, R. T. Sam and P. Verma, *Appl. Phys. Lett.*, 2019, **114**, 073105.
55 J. Liao, J. Wu, C. Dang and L. Xie, *Acta Phys. Sin.*, 2021, **70**, 028201–028201.
56 X. Xin, Y. Zhang, J. Chen, M. Chen, W. Xin, M. Ding, Y. Bao, W. Liu, H. Xu and Y. Liu, *Mater. Horiz.*, 2022, **9**, 2416–2424.
57 Y. Okuno, O. Lancry, A. Tempez, C. Cairone, M. Bosi, F. Fabbri and M. Chaigneau, *Nanoscale*, 2018, **10**, 14055–14059.
58 C. Lee, B. G. Jeong, S. H. Kim, D. H. Kim, S. J. Yun, W. Choi, S.-J. An, D. Lee, Y.-M. Kim, K. K. Kim, S. M. Lee and M. S. Jeong, *npj 2D Mater. Appl.*, 2022, **6**, 67.
59 R. Kato, T. Moriyama, T. Umakoshi, T.-a. Yano and P. Verma, *Sci. Adv.*, 2022, **8**, eabo4021.
60 D. Wu, X. Li, L. Luan, X. Wu, W. Li, M. N. Yogeesh, R. Ghosh, Z. Chu, D. Akinwande, Q. Niu and K. Lai, *Proc. Natl. Acad. Sci. U. S. A.*, 2016, **113**, 8583–8588.
61 V. Carozo, Y. Wang, K. Fujisawa, B. R. Carvalho, A. McCreary, S. Feng, Z. Lin, C. Zhou, N. Perea-Lopez, A. L. Elias, B. Kabius, V. H. Crespi and M. Terrones, *Sci. Adv.*, 2017, **3**, e1602813.
62 A. Rodriguez, T. Verhagen, M. Kalbac, J. Vejpravova and O. Frank, *Phys. Status Solidi RRL*, 2019, **13**, 1900381.
63 T. X. Huang, X. Cong, S. S. Wu, K. Q. Lin, X. Yao, Y. H. He, J. B. Wu, Y. F. Bao, S. C. Huang, X. Wang, P. H. Tan and B. Ren, *Nat. Commun.*, 2019, **10**, 5544.
64 D. Wang, H. Yu, L. Tao, W. Xiao, P. Fan, T. Zhang, M. Liao, W. Guo, D. Shi, S. Du, G. Zhang and H. Gao, *Nano Res.*, 2018, 8583–8588.
65 Y. L. Huang, Y. Chen, W. Zhang, S. Y. Quek, C.-H. Chen, L.-J. Li, W.-T. Hsu, W.-H. Chang, Y. J. Zheng, W. Chen and A. T. S. Wee, *Nat. Commun.*, 2015, **6**, 6298.
66 S. Sheng, J.-b. Wu, X. Cong, W. Li, J. Gou, Q. Zhong, P. Cheng, P.-h. Tan, L. Chen and K. Wu, *Phys. Rev. Lett.*, 2017, **119**, 196803.
67 J. Jelken, M. O. Avilés and F. Lagugné-Labarthet, *ACS Nano*, 2022, **16**, 12352–12363.
68 S. Kataria, S. Wagner, T. Cusati, A. Fortunelli, G. Iannaccone, H. Pandey, G. Fiori and M. C. Lemme, *Adv. Mater. Interfaces*, 2017, **4**, 1700031.
69 S. B. Desai, G. Seol, J. S. Kang, H. Fang, C. Battaglia, R. Kapadia, J. W. Ager, J. Guo and A. Javey, *Nano Lett.*, 2014, **14**, 4592–4597.
70 Z. J. Zhang, A. C. De Palma, C. J. Brennan, G. Cossio, R. Ghosh, S. K. Banerjee and E. T. Yu, *Phys. Rev. B*, 2018, **97**, 085305.
71 A. G. Milekhin, M. Rahaman, E. E. Rodyakina, A. V. Latyshev, V. M. Dzhagan and D. R. T. Zahn, *Nanoscale*, 2018, **10**, 2755–2763.
72 M. Rahaman, R. D. Rodriguez, G. Plechinger, S. Moras, C. Schüller, T. Korn and D. R. T. Zahn, *Nano Lett.*, 2017, **17**, 6027–6033.
73 Y. Koo, Y. Kim, S. H. Choi, H. Lee, J. Choi, D. Y. Lee, M. Kang, H. S. Lee, K. K. Kim, G. Lee and K. D. Park, *Adv. Mater.*, 2021, **33**, 2008234.
74 C. Carmesin, M. Lorke, M. Florian, D. Erben, A. Schulz, T. O. Wehling and F. Jahnke, *Nano Lett.*, 2019, **19**, 3182–3186.
75 T. P. Darlington, C. Carmesin, M. Florian, E. Yanev, O. Ajayi, J. Ardelean, D. A. Rhodes, A. Ghiotto, A. Krayev, K. Watanabe, T. Taniguchi, J. W. Kysar, A. N. Pasupathy, J. C. Hone, F. Jahnke, N. J. Borys and P. J. Schuck, *Nat. Nanotechnol.*, 2020, **15**, 854–860.
76 A. Rodriguez, A. Krayev, M. Velický, O. Frank and P. Z. El-Khoury, *J. Phys. Chem. Lett.*, 2022, **13**, 5854–5859.
77 A. Rodriguez, M. Kalbac and O. Frank, *2D Mater.*, 2021, **8**, 025028.
78 A. Albagami, S. Ambardar, H. Hrim, P. K. Sahoo, Y. Emirov, H. R. Gutierrez and D. V. Voronine, *ACS Appl. Mater. Interfaces*, 2022, **14**, 11006–11015.
79 J. Liu, W. Xue, H. Zong, X. Lai, P. Sahoo, H. R. Gutierrez and D. Voronine, 2017, arXiv:1711.11166, DOI: **10.48550/arXiv.1711.11166**.
80 P. K. Sahoo, H. Zong, J. Liu, W. Xue, X. Lai, H. R. Gutiérrez and D. V. Voronine, *Opt. Mater. Express*, 2019, **9**, 1620–1631.

 This journal is © The Royal Society of Chemistry 2022

81 J. Q. Shao, F. Chen, W. T. Su, Y. J. Zeng and H. W. Lu, *ACS Appl. Mater. Interfaces*, 2021, **13**, 20361–20370.
82 S. Garg, J. P. Fix, A. V. Krayev, C. Flanery, M. Colgrove, A. R. Sulkanen, M. Y. Wang, G. Y. Liu, N. J. Borys and P. Kung, *ACS Nano*, 2022, **16**, 340–350.
83 A. Krayev, P. Chen, H. Terrones, X. Duan, Z. Zhang and X. Duan, *J. Phys. Chem. C*, 2022, **126**, 5218–5223.
84 Z. He, Z. H. Han, J. T. Yuan, A. M. Sinyukov, H. Eleuch, C. Niu, Z. R. Zhang, J. Lou, J. Hu, D. V. Voronine and M. O. Scully, *Sci. Adv.*, 2019, **5**, eaau8763.
85 D. Jariwala, A. Krayev, J. Wong, A. E. Robinson, M. C. Sherrott, S. Wang, G. Y. Liu, M. Terrones and H. A. Atwater, *2D Mater.*, 2018, **5**, 035003.
86 C. Tang, Z. He, W. Chen, S. Jia, J. Lou and D. V. Voronine, *Phys. Rev. B*, 2018, **98**, 041402.

Published on 17 November 2022. Downloaded by Yunnan University on 8/14/2025 5:32:42 PM.